Food Science of Animal Resources
Food Sci. Anim. Resour. 2025 November 45(6):1620~1643
DOI https://doi.org/10.5851/kosfa.2024.e135
pISSN : 2636-0772 eISSN : 2636-0780
http://www.kosfaj.org

ARTICLE

Coacervates of Lactoferrin with Resistant Dextrin via Noncovalent Interaction for Enhanced Thermal Stability, Interface Characteristics and Docosahexaenoic Acid (DHA) Encapsulation

Juanjuan Luo, Ning Wang, Haohui Li, Junnan Wan, Yiting Zhao, Hua Jiang, Cunfang Wang*, and Xiaoning Zhang*

College of Food Science and Engineering, Qilu University of Technology (Shandong Academy of Sciences), Jinan 250353, China

OPEN ACCESS

Received September 5, 2024
Revised December 17, 2024
Accepted December 19, 2024

*Corresponding author :
Cunfang Wang
College of Food Science and Engineering, Qilu University of Technology (Shandong Academy of Sciences), Jinan 250353, China
Tel: +86-183-5310-8782
Fax: +86-0531-89631195
E-mail: cunfangwang@163.com

Xiaoning Zhang
College of Food Science and Engineering, Qilu University of Technology (Shandong Academy of Sciences), Jinan 250353, China
Tel: +86-183-5315-3161
Fax: +86-0531-89631195
E-mail: xiaoningzhang@126.com

*ORCID
Juanjuan Luo
https://orcid.org/0009-0008-1219-3096
Ning Wang
https://orcid.org/0009-0004-8446-1441
Haohui Li
https://orcid.org/0009-0009-4603-6408
Junnan Wan
https://orcid.org/0009-0002-2195-8640
Yiting Zhao
https://orcid.org/0009-0008-5574-859X
Hua Jiang
https://orcid.org/0000-0003-0013-7173
Cunfang Wang
https://orcid.org/0000-0001-7992-6524
Xiaoning Zhang
https://orcid.org/0000-0002-5914-5437

Abstract Lactoferrin (LF), resistant dextrin (RD), and docosahexaenoic acid (DHA) are critical functional components in infant formula. However, LF exhibits thermally unstable, and DHA is susceptible to degradation from exposure to light, heat, and oxygen. The coacervation of LF with RD through the electrostatic interactions may be an effective strategy for addressing these issues. This study aimed to investigate the coacervation conditions and thermodynamic formation mechanism of LF with RD to improve the thermal stability and interfacial properties of LF, alongside assessing the feasibility of embedding DHA after LF coacervates with RD. The optimal coacervation conditions for LF with RD were identified to be pH 7.0 and an LF-to-RD mass ratio of 1:12. LF-RD complex coacervation was thermodynamically favored ($\Delta G<0$), attributed to entropy gain ($\Delta S>0$) and negative enthalpy change ($\Delta H<0$). Following coacervation with RD, the thermal stability of LF was improved due to noncovalent interactions. The process of complex coacervation also enhanced the surface hydrophobicity, as well as the emulsifying and foaming capabilities of LF. Optical microscopy and confocal laser scanning microscopy results indicate that, following complex coacervation, DHA droplets are uniformly dispersed within the emulsion, exhibiting a spherical shape with a denser wall forming around them. Additionally, DHA has been successfully encapsulated by LF-RD complex coacervates, with an encapsulation efficiency reaching 89.5%. This study provides a reference for enhancing the thermal stability and functionality of LF in the food industry and offers insights into the further application of LF-RD complexes and DHA microcapsules in infant formula.

Keywords complex coacervation, lactoferrin, noncovalent interaction, thermal stability, docosahexaenoic acid (DHA) microcapsule

Introduction

As an alternative to breast milk, infant formula has achieved an annual growth rate of nearly 20% since 2013 in the global market, particularly in China (Meng et al., 2024).

Lactoferrin (LF), a prominent bioactive glycoprotein found in human milk, is also present in animal milk and exerts a variety of beneficial effects. Research indicates that it plays an important role in safeguarding infants against infections, facilitating the development of the immune system, and ameliorating iron deficiency anemia in infants (Hao et al., 2019). Given its excellent biological functions, LF is frequently incorporated into infant formula to enhance the nutritional profile of milk powder, thereby making it more comparable to breast milk. However, LF is susceptible to various environmental factors, including thermal processing, pH levels, and ionic strength, which can cause protein denaturation, disrupt the spatial configuration of LF, and ultimately result in a loss of its biological functions. The complex coacervation of LF and polysaccharides is considered a promising approach for protecting LF from thermal denaturation, primarily owing to its avoidance of elevated temperatures and organic solvents. Previous studies have shown that the thermal stability of LF can be enhanced through complex coacervation with anionic polysaccharides, such as soybean soluble polysaccharide, okra polysaccharide, and sodium alginate (Li et al., 2019; Lin et al., 2022; Xu et al., 2019). Moreover, these complex coacervates play a key role in regulating food structure, stabilizing emulsions, substituting fats, and encapsulating bioactive ingredients (Ahad et al., 2023; Krzeminski et al., 2014; Warnakulasuriya and Nickerson, 2018).

Resistant dextrin (RD) is a typical oligosaccharide widely present in infant formula, recognized for its properties such as low viscosity, high solubility in water, and unique thermal stability, which render it a preferred component in functional foods and beverages (Trithavisup et al., 2019). Docosahexaenoic acid (DHA) serves as a nutritional fortifier in infant formula, and a recent regulation from the European Commission mandates its inclusion in such products. DHA is associated with several biological benefits, such as the promotion of brain and visual development, the prevention of cardiovascular diseases, and potential anti-cancer effects (Fu et al., 2020). However, DHA is susceptible to degradation through exposure to oxygen, light and heat, which can lead to oxidation and the development of off-putting odors during the production and storage of infant formula (Wang et al., 2022). Microencapsulation of DHA presents a viable technological approach to protect it from oxidative degradation. This method can not only preserve the nutrient's integrity and extends its shelf life, but also helps to mask undesirable flavors. Research conducted by Chen et al. (2016) demonstrated that encapsulating DHA within a wall matrix composed of a glucose, casein, and lactose yields microcapsules with remarkable oxidative stability. Following accelerated oxidation tests at 45℃ over a period of 8 weeks, the peroxide value of the encapsulated DHA was found to be merely one-ninth of the unencapsulated DHA oil.

To the best of our knowledge, there is a paucity of research on the effects of LF and RD complex coacervation on the functional properties of LF, particularly in the context of utilizing LF-RD complexes as carriers for the delivery of DHA. The formation of complex coacervates between proteins and polysaccharides is primarily driven by electrostatic attractions between the charged groups present on these macromolecules (Tian et al., 2023). The strength of these interactions is influenced by various factors, including pH, the ratios of biopolymers, and ionic strength (Liu et al., 2009; Samanta and Ganesan, 2018). Thus, it is essential to identify the optimal conditions for the complex coacervation process. Moreover, the electrostatic complexes generated through the coacervation of proteins and polysaccharides not only integrate the unique physicochemical properties of both components, but also provide a viable strategy to address the limitations and improve functionality of individual biopolymers, thereby indicating a broader potential for application (Bastos et al., 2018; Meng et al., 2024; Xu et al., 2020).

On the background of this, this study was designed to (1) identify the optimal conditions (pH, biopolymer mixing ratios) for the formation of LF-RD complex coacervates; (2) determine the binding constant, number of binding sites, and thermodynamic parameters for this complex reaction under different temperatures; (3) characterize the structural, thermal,

foaming, emulsifying, morphological, antioxidant, and *in vitro* digestion properties of LF-RD complex coacervates; (4) explore the feasibility of microencapsulating DHA using LF-RD complex coacervates.

Materials and Methods

Materials

Bovine LF (purity≥95.0%), DHA, Nile blue, Nile red, 5-aminofluorescein, dimethyl sulfoxide, and gallic acid (GA) were provided by Shanghai Yuanye Bio-Technology (Shanghai, China). RD was sourced from Shandong Balongchuangyuan Bio-Technology (Shandong, China). Hydrochloric acid (HCl), 8-anilino-1-naphthalenesulfonic acid (ANS), sodium hydroxide (NaOH), and 2, 2-diphenyl-1-picrylhydrazyl (DPPH), were procured from Sigma-Aldrich® (Shanghai, China).

Preparation of lactoferrin, resistant dextrin and lactoferrin-resistant dextrin complex coacervates solutions

Add LF and RD powders to distilled water separately to a concentration of 0.1% (w/w). The preparation of complex coacervates involved mixing LF and RD powders in various mass ratios (LF:RD=1:1, 1:2, 1:4, 1:8, 1:12, 1:16, 1:20, w/w), and the total concentration of the mixed solution formed was 0.1%. Subsequently, these solutions were homogenized through a magnetic stirrer (RO10, IKA, Staufen, Germany) for 2 h to ensure absolute dissolution.

Determination of the zeta potential, particle size and turbidity

A Zetasizer Nano (Nano-ZS, Malvern Instruments, Malvern, UK) was conducted to measure the zeta potential and particle size of LF, RD, and LF-RD coacervates. Samples' pH was adjusted within a range of 4.0 to 8.5 by adding 0.1 M HCl and 0.1 M NaOH in increments of 0.5±0.05 units. The zeta potentials of LF and RD measured at each pH were labeled as ZP_1 and ZP_2, respectively. Then, the strength of the electrostatic interaction (SEI) between LF and RD was calculated using Eq. (1) (Tomé Constantino and Garcia-Rojas, 2022).

$$\text{SEI } (\text{mV}^2) = |\text{ZP}_1| \times |\text{ZP}_2| \quad (1)$$

The determination of turbidity for samples at pH 7.0 was performed using a spectrophotometer (UV-2550, Shimadzu, Kyoto, Japan). Distilled water served as the reference and the samples' turbidity was represented as absorbance at 600 nm.

Measurement of the coacervate yield

The yield of coacervates from the systems (1%, w/v) was assessed at various ratios of LF to RD (1:1, 1:2, 1:4, 1:8, 1:12, 1:16, and 1:20, w/w) according to Chen et al. (2021). Simply, once the complex coacervate was formed at the optimum pH (highest turbidity), centrifugation was carried out, and the precipitate obtained was dried at 105±0.1℃. The dried complex coacervates' weight, as well as the total weight of LF and RD, were recorded as Wc and Wt, respectively. Then, the yield of the complex coacervates was estimated by the Eq. (2).

$$\text{Complex coacervate yield } (\%) = \frac{W_c}{W_t} \times 100 \quad (2)$$

Preparation of the lactoferrin-resistant dextrin coacervates

Based on the trials conducted in the previous section of 2.3, 2.4, and 2.5 in this study, a mixed solution of LF-RD (0.1%, w/w) with a ratio of LF to RD at 1:12 was employed to produce complex coacervates. The blend was mixed thoroughly and its pH was corrected to 7.0. Subsequently, the mixed solution's temperature was quickly lowered to below 5℃ in an ice bath and stirred at 200 rpm for 30 min to enhance coacervate formation. The resulting solution was freeze-dried using a lyophilizer (Freezone® 6 Plus, Labconco, Kansas City, MO, USA) for subsequent analysis.

Intrinsic fluorescence spectrum

Fluorescence spectroscopy was performed at three distinct temperatures (298 K, 303 K, and 308 K) by a fluorescence spectrophotometer (F-2700, Hitachi, Tokyo, Japan). The interaction between LF and RD was confirmed through the fluorescence quenching method as described by Li et al. (2018) with slight amendments. Various concentrations of RD solutions were introduced to the LF solution, resulting in a final concentration of LF was12.5 μM, while RD's final concentrations were 20, 40, 80, 160, 240, 320, and 400 μM, respectively. Fluorescence spectra were recorded in the 300–450 nm range at an excitation wavelength of 295 nm.

The binding constant (Ka) and the number of binding sites (n) of the binding characteristics between LF and RD were calculated according to the double logarithmic Eq. (3) (Yan et al., 2022).

$$\mathrm{Log}\left[\frac{F_0-F}{F}\right] = \mathrm{Log\ Ka} + n\ \mathrm{Log}\,[RD] \tag{3}$$

In this equation, F_0 and F stand for the maximum fluorescence intensity of LF without RD and with RD; while [RD] represents the concentration of RD.

To investigate the thermodynamical parameters, the enthalpy change (ΔH), entropy change (ΔS), and Gibbs free energy change (ΔG) were calculated according to the Van't Hoff equation.

$$\ln \mathrm{Ka} = -\frac{\Delta H}{RT} + \frac{\Delta S}{R} \tag{4}$$

$$\Delta G = \Delta H - T\Delta S \tag{5}$$

Here, R denotes the gas constant (8.314 J mol^{-1} K^{-1}) and T signifies the thermodynamic temperature (298 K, 304 K, or 310 K).

Fourier transform infrared and X-ray diffractogram

Structural analysis of LF, RD, and lyophilized coacervate was conducted utilizing an Fourier transform infrared (FTIR) spectrometer (Nicolet iS10, Thermo Fisher Scientific, Waltham, MA, USA). Spectral data were collected over a wavelength range from 4,000 to 600 cm^{-1}.

The diffraction patterns of LF, RD, and lyophilized coacervate were analyzed using a wide-range X-ray diffractometer (D8 ADVANCE, Bruker, Germany) with Cu-Kα radiation (λ=1.54056 A°). The sample was positioned on a flat glass sample holder and scanned in reflection mode at a scanning rate of 0.02° 2θ/s within the 4°–40° range. All measurements were conducted at a 40 kV voltage and 40 mA tube current.

Morphology of lactoferrin-resistant dextrin coacervates

Scanning electron microscopy (SEM) was done to observe the shape and morphology of LF, RD, and LF-RD coacervates. Samples were initially affixed onto a conductive adhesive and then covered with a gold layer through a spraying process. Subsequently, the morphology was observed at various magnification levels using a scanning electron microscope (GeminiSEM 300, ZEISS, Oberkochen, Germany).

To achieve confocal laser scanning microscopy (CLSM) investigations, the sample solution (0.01% and 1%, w/v) was stained with a mixed fluorescent dye solution composed of 1.0 mg mL^{-1} Nile blue and 1.0 mg mL^{-1} 5-aminofluorescein for 20 min at 25℃. Subsequently, 5 μL of the sample solution was placed on a glass slide and examined by 20× objective lens on a confocal laser scanning microscope (Olympus FV 1200-BX61, Olympus, Tokyo, Japan). Nile blue and 5-aminofluorescein observations were obtained at laser wavelengths of 633 and 488 nm, respectively.

Surface hydrophobicity

The surface hydrophobicity was assessed according to Zhang et al. (2024). Briefly, a 20 μL solution of 8 mM ANS, which served as a hydrophobic probe, was added to a 4 mL sample solution. After a 15-minute incubation period in the dark, fluorescence spectroscopy was then conducted, with excitation was 390 nm and emission wavelengths was 400 to 600 nm.

Foaming and emulsifying properties

The foaming characteristics of samples were analyzed by Yan et al. (2022), albeit with minor adjustments. Specifically, the foam was accomplished by agitating a 10 mL sample solution (10 mg mL^{-1}) at a high speed (10,000 r min^{-1}) for 2 min. The calculation formula of foam capacity (FC) and foam stability (FS) were as stated below:

$$\text{FC}\ (\%) = \frac{V_0 - V}{V} \times 100 \quad (6)$$

$$\text{FS}\ (\%) = \frac{V_{30}}{V_0} \times 100 \quad (7)$$

Where V (mL) represents the initial volume pro-homogenization; V_0 (mL) and V_{30} (mL) refer to the foam volumes at 0 min and 30 min post-homogenization, respectively.

A mixture comprising the sample solution (1 mg mL^{-1}) and olive oil (3:1, v/v) was subjected to homogenization at a speed of 12,000 r min^{-1} for a duration of 3 min. Subsequently, emulsions (30 μL each) were collected at 0 and 10 minutes and mixed with 3 mL of 0.1% (w/v) sodium dodecyl sulfate solution. The absorbance values of samples were measured at 500 nm. The emulsion activity index (EAI) and emulsification stability index (ESI) were determined utilizing the provided formulas:

$$\text{EAI}\ (m^2/g) = \frac{2.303 \times 2 \times A_0 \times N}{10{,}000 \times C \times \varphi} \quad (8)$$

$$\text{ESI}\ (\text{min}) = \frac{A_0}{A_0 - A_{10}} \times 10 \quad (9)$$

Here, N is the dilution factor (100); C stands for the LF concentration (g mL^{-1}); φ indicates the volume fraction of oil in the emulsions; A_0 and A_{10} refer to the absorbances measured at 0 and 10 min respectively.

Differential scanning calorimetry and thermogravimetric

A differential scanning calorimetry (DSC; Discovery DSC-250, TA Instruments, New Castle, DE, USA) was employed to characterize the thermal stability of the samples. Sealed aluminum pans containing lyophilized samples (5–10 mg) were heated from 30℃ to 180℃ at a rate of 5℃ min^{-1}. The thermal stability of LF, RD, and lyophilized complexes was explored utilizing a thermogravimetric (TGA) analyzer (TGA2, Mettler-Toledo, Schwerzenbach, Switzerland). Typically, 5–10 mg of sample was subjected to heating from 30℃ to 600℃ at a rate of 10℃ min^{-1}.

Determination of antioxidant activity

According to the methods outlined in the Chinese national standard (Ministry of Health of the People's Republic of China, 2020) and the previous reports (Chen et al., 2022; Li et al., 2021a; Li et al., 2023), the antioxidant activity of the LF-RD complex coacervates was assessed using the DPPH and 2,2'-azino-bis(3-ethylbenzothiazoline-6-sulfonic acid) (ABTS) assays. In the DPPH assay, 1 mL of a 2 mg mL^{-1} sample solution was mixed with 3 mL of 0.1 mM ethanol DPPH solution. The samples were then incubated in the dark for 30 min, after which the absorbance was measured at 517 nm by a UV/visible spectrophotometer (UV-2550, Shimadzu). For the ABTS assay, a 7.0 mM ABTS solution was mixed with a 2.45 mM potassium persulfate solution and stored in the dark for 16 h. The resulting mixture was diluted with distilled water to obtain an absorbance of 0.70±0.02 at 734 nm. The samples were then combined with an equal volume of ABTS stock solution and allowed to react for 30 min, with absorbance subsequently measured at 734 nm. The radical scavenging activity (%) was calculated using the following formula:

$$\text{Radical scavenging activity (\%)} = \frac{A - (A_1 - A_2)}{A} \times 100 \quad (10)$$

Here, A denotes the absorbance of the control sample, A_1 represents the absorbance of the sample after 30 min of reaction in the dark, and A_2 corresponds to the absorbance of the sample without DPPH or ABTS.

GA was utilized as a standard control in the antioxidant activity assays to establish standard curves for DPPH and ABTS radicals. A stock solution was prepared by dissolving 1.89 mg of GA in 25 mL distilled water, which was subsequently diluted to obtain GA solutions with concentrations varying from 10 to 80 μM and 20 to 100 μM. These solutions were then subjected to reactions with DPPH and ABTS radicals, as previously described, and the absorbance was recorded at 517 nm and 734 nm, respectively. Standard curves were developed by plotting the concentrations of GA against their corresponding absorbance values. Following this, 5 mg mL^{-1} solutions of LF, RD, and LF-RD complexes were subjected to DPPH and ABTS radical scavenging assays using the same procedure. The results were expressed as μmol gallic acid equivalent (GAE)/g sample.

In vitro simulation of gastric digestion

An *in vitro* digestion pattern was employed to analyze the gastric digestion process of LF and LF-RD complex coacervates,

with the simulated gastric fluid prepared following previously reported methods (Ménard et al., 2018). Specifically, the infant simulated gastric fluid was composed of NaCl (94 mM) and KCl (13 mM), with the pH adjusted to 5.3 using 1 M HCl. The LF concentration was set at 5 mg mL^{-1}, and the samples were digested with pepsin at a ratio of 268 U mL^{-1}. *In vitro* digestion was initiated by adding 5 mL of pre-warmed (37°C) simulated gastric fluid to 5 mL of the sample solution. Samples were collected at 0, 30, 60, and 120 min after the initiation of digestion. Subsequently, the hydrolysis of LF and LF-RD complexes during this simulated digestion was assessed through sodium dodecyl sulfate-polyacrylamide gel electrophoresis, which was performed using a 5% concentrate gel and a 12% separator gel at 120 V for 2 h. After electrophoresis, the gels were stained with Coomassie Brilliant Blue R-250 (Solarbio, Beijing, China) for 2 h and then destained overnight in a 7.5% acetic acid.

Preparation of docosahexaenoic acid microcapsules and determination of encapsulation efficiency

The encapsulation process was carried out according to El Ghazzaqui Barbosa et al. (2022) with minor adaptations. To this end, the solution contained 1.0% (w/w) wall material with a core-to-wall ratio of 1:2 (w/w). Initially, an oil-in-water emulsion was prepared using an Ultra-Turrax (Ultraturrax T18, IKA) with LF and DHA at 10,340×g for 5 min. Subsequently, RD was added to the emulsions, adjusting the pH to 7.0 with 0.1M HCl. Transglutaminase (30 U/g of protein) was introduced to facilitate the crosslinking of the wall material. Finally, samples were frozen in liquid nitrogen and lyophilized. Regarding the encapsulation efficiency of DHA microcapsules, it was assessed following the method described by Chen et al. (2022). This involves measuring the surface oil (SO) and total oil (TO) contents by gravimetric method, and the encapsulation efficiency was calculated according to Eq. (11).

$$\text{Encapsulation efficiency (\%)} = \frac{W_{TO} - W_{SO}}{W_{TO}} \times 100 \quad (11)$$

Morphological observation of docosahexaenoic acid microcapsules

The encapsulation process of DHA microcapsules was observed under an optical microscope. The sample was positioned at the center of a glass slide and carefully covered with a coverslip. DHA was stained with Nile red, and the formation of microcapsules was monitored by an optical microscope fitted with a camera (CX 21, Olympus). The CLSM observations of DHA microcapsules was referred to those of LF-RD complexes, as detailed in section 2.8, with the sole distinction being the use of Nile red for staining DHA instead of 5-aminofluorescein.

Statistical analysis

All the data obtained from three parallel experiments were presented as the mean±SD. An analysis of variance (ANOVA) was performed using Duncan's multiple range test ($p<0.05$), facilitated by SPSS 25.0 software (IBM, Armonk, NY, USA). Graphical illustrations were generated using Origin 2018 software (OriginLab, Northampton, MA, USA).

Results and Discussion

Effect of pH and ratio on the formation of the lactoferrin-resistant dextrin complex coacervates

The coacervation of protein-polysaccharide complex is driven by electrostatic forces between biopolymers possessing contrasting charges. This process is significantly influenced by pH, which exerts a substantial influence on this process by

modulating the intensity of electrostatic attraction and the degree of complex coacervation between the biopolymers (Chen et al., 2021). In addition, the proportion of protein to polysaccharide in the mixture is another critical variable that impacts the results, as an ideal ratio fosters heightened electrostatic interactions and maximizes coacervate yield (Chen et al., 2022; Li et al., 2024). Hence, this study commenced by establishing the optimal pH and LF to RD ratio as fundamental parameters.

Fig. 1A illustrates the variations in the zeta potential values of LF and RD in the pH range of 4.0–8.5. It is evident that as the pH increased, the zeta potential values for both LF and RD tended to decrease. The isoelectric point (pI) of LF is approximately 8.2, consistent with previous research findings (Peinado et al., 2010). The zeta potential value of RD became positive below pH 4.7, whereas it remained negatively charged at all pH values above 4.7. SEI was calculated based on the zeta potential values of

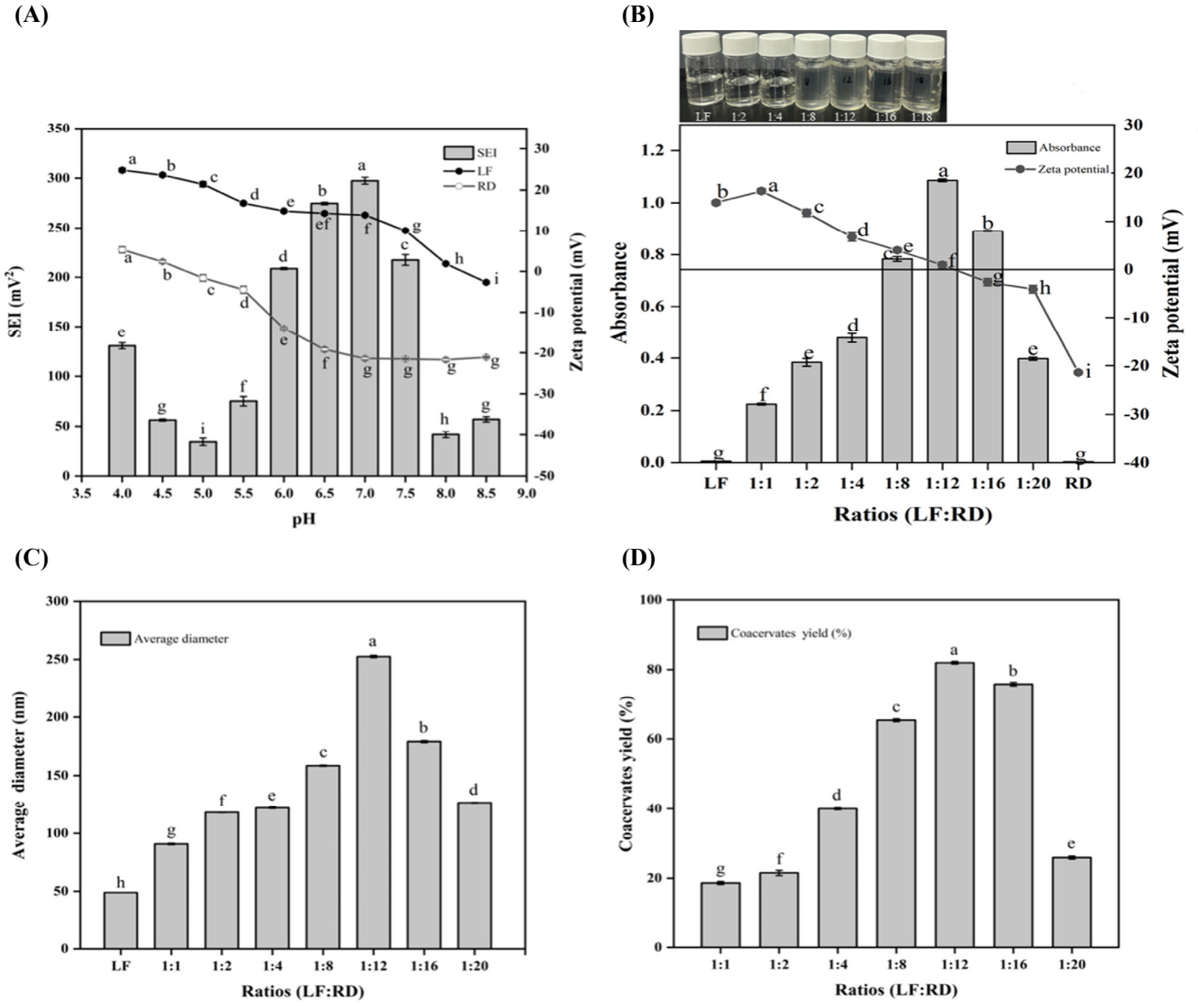

Fig. 1. Effects of pH and ratios on LF-RD complex coacervation. (A) Zeta potential and SEI of biopolymers (LF and RD) at different pH values. (B) Effect of LF-to-RD ratios on the zeta potential and turbidity at a fixed pH (pH 7.0). Images depicting the visual characteristics of mixed solutions of LF and RD at varying weight ratios (LF:RD, w/w). (C) The average diameter of LF and different LF-to-RD ratios at pH 7.0. (D) Coacervate yield at pH 7.0 and different LF-to-RD ratios. Error bars represent±SD, n=3. $^{a–i}$ The lowercase letters depicted in the figure denote statistically significant differences ($p<0.05$) among the various samples for each indicator. SEI, strength of the electrostatic interaction; LF, lactoferrin; RD, resistant dextrin.

LF and RD. Electrostatic interaction forces are significant in determining the optimal pH for interactions between biopolymers. The highest SEI of 297.46±3.41 mV^2 was observed at pH 7.0, suggesting the strongest binding or attraction between LF and RD. This parameter is crucial for complex coacervation, given that RD carries a negative charge above pH 4.7 and LF is positively charged below pH 8.2. Similar findings have also been observed that LF can form complex coacervates with soy protein isolate, okra polysaccharide, or sodium alginate at a neutral pH value (Tokle et al., 2010; Xu et al., 2019; Zheng et al., 2020). Thus, this pH value was used to identify the most appropriate LF-to-RD ratio.

The zeta potential and turbidity results for various LF:RD ratios (1:1–1:20, w/w) at pH 7.0 are presented in Fig. 1B. It was noted that neither LF nor RD solutions exhibited turbidity at pH 7.0, indicating the absence of self-aggregation. With an increase in the RD content, the turbidity of the system gradually increased, peaking at an LF:RD ratio of 1:12. At this ratio, the zeta potential was closest to electrical neutrality (0.91 mV), implying that an equilibrium between positive (NH_3^+) and negative (COO^-) charges was attained. Comparable results were documented in a research study that investigated the combination of LF and carboxymethyl tara gum in different ratios (Santos et al., 2021). However, a further rise in the RD content resulted in a reduction in turbidity. Studies have proposed that an excessive amount of polysaccharides in the system impedes protein aggregate formation by inducing steric repulsion, thereby reducing turbidity (Naderi et al., 2020).

Fig. 1C displays the average diameters of the LF and LF-RD coacervate at pH 7.0. Initially, the average diameter of the LF at room temperature is 48.96±0.02 nm. Following the addition of RD, the average diameter of the LF-RD complex exhibited a gradual increase, which may be potentially ascribed to electrostatic interactions between LF and RD molecules. The particle size achieved a maximum value of 252.6±1.08 nm at a ratio of 1:12, signifying the optimal degree of complex coacervation of LF and RD under these specific conditions. A similar trend was noted in a previous investigation, where the diameter of the LF-NaCas complex increased with an escalating NaCas addition ratio ranging from 4:1 to 1:2 (LF: NaCas, w/w; Li and Zhao, 2017).

In order to identify the optimal conditions for complex coacervation, specifically focusing on a 1:12 ratio and a pH of 7.0, the coacervate yield was assessed. The results presented in Fig. 1D indicate that the highest coacervate yield is achieved at pH 7.0 and a 1:12 ratio, which aligns with the findings from the turbidity measurements. Taking into account a comprehensive analysis of the experimental results presented above, it can be inferred that a 1:12 (LF:RD) ratio at pH 7.0 is the most favorable condition for the generation of complex coacervates.

Intrinsic fluorescence spectroscopy

Fluorescence spectroscopy serves as a prevalent method for investigating the interactions that occur between proteins and bioactive substances (Rossi and Taylor, 2011; Zhang et al., 2020). Figs. 2A, B, and C depicts the changes in the intrinsic fluorescence intensity of LF as a function of RD concentration. It was observed that under pH 7.0 conditions, LF exhibited a maximum intrinsic fluorescence emission at approximately 331.5 nm, in compliance with a previous study (Li et al., 2019). The fluorescence intensity of LF demonstrated a concentration-dependent decay as RD concentration increased, a trend similarly noted by Peinado et al. (2010). The finding implies that the intrinsic fluorescence of LF is quenched due to the complexation interaction between LF and RD.

To elucidate the binding characteristics of the LF-RD complexes, the double logarithmic equation [Eq. (3)] was employed to determine the Ka and n, as outlined in Table 1. Analysis revealed a negative correlation between Ka values and temperature increase (298 K: 8.73×10^4 L mol^{-1}, 303 K: 8.22×10^4 L mol^{-1}, 308 K: 7.83×10^4 L mol^{-1}), implying that the high temperature is not conducive to the interaction between LF and RD. Interestingly, fluctuations in temperature had minimal impact on the

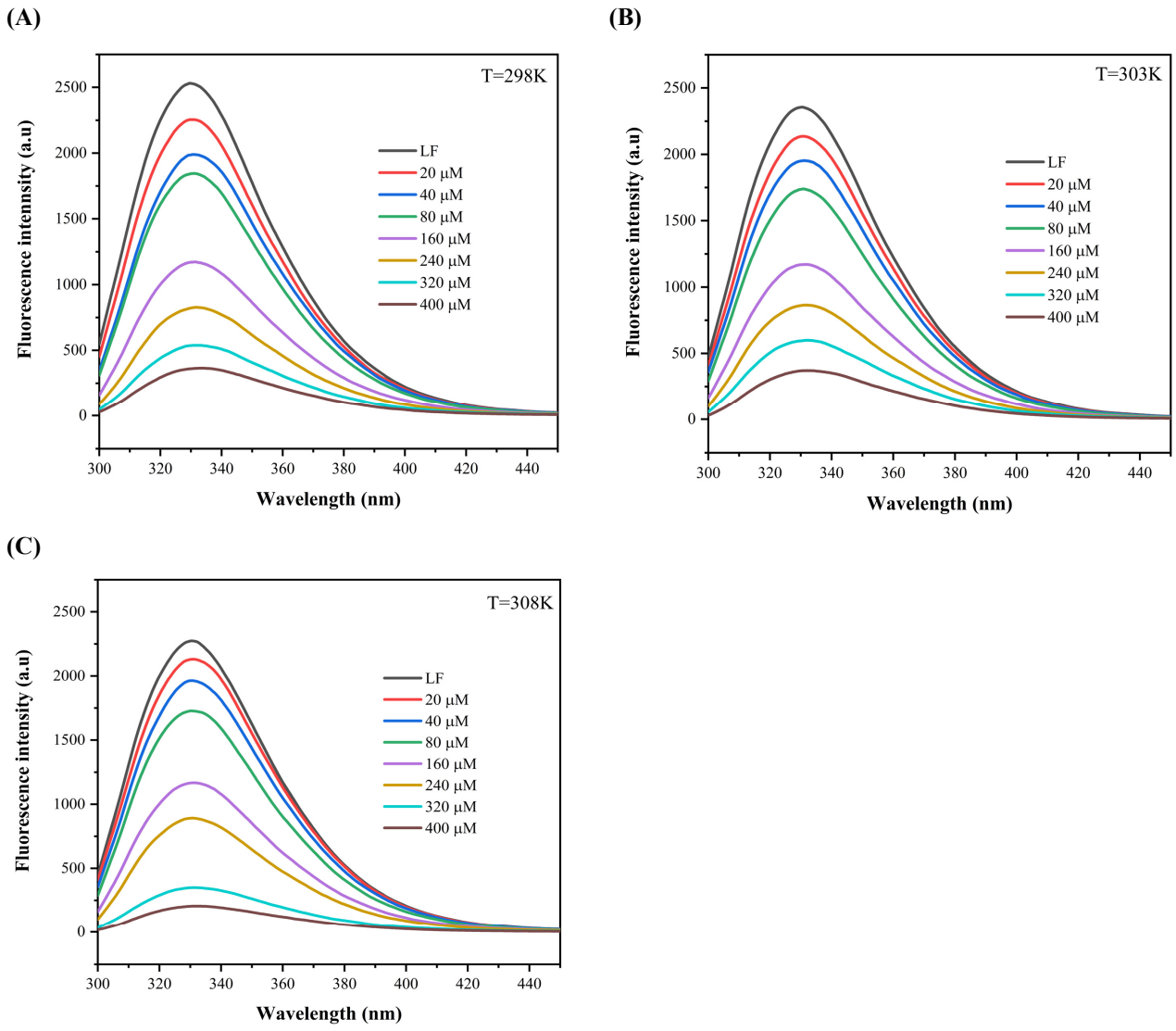

Fig. 2. Fluorescence emission spectra of LF (12.5 μM) with various concentrations of RD (20–400 μM) at (A) 298 K, (B) 303 K, and (C) 308 K. LF, lactoferrin; RD, resistant dextrin.

Table 1. Binding affinities (Ka), numbers of the binding sites (n), and thermodynamic parameters of the binding interaction between LF and RD at 298 K, 303 K, and 308 K

T (K)	Ka ($\times 10^4$ M^{-1})	n	△G (KJ mol^{-1})	△H (KJ mol^{-1})	△S (J mol^{-1} K^{-1})
298	8.73	1.282	− 28.49	− 8.49±0.33	66±2
303	8.22	1.272			
308	7.83	1.247			

LF, lactoferrin; RD, resistant dextrin.

value of n, which remained close to 1. A study by Yan et al. (2022) also reported similar results for n in cases where LF was non-covalently bound to Re/Rb_1.

Thermodynamic parameters were employed to elucidate the driving forces that govern the interaction between LF and RD. By applying the Van't Hoff equation [Eqs. (4) and (5)], the values ΔG, ΔH, and ΔS were determined, with detailed

information provided in Table 1. The negative value of ΔG implies the spontaneous occurrence of the LF-RD combination. Furthermore, the complex exhibited a ΔH of –8.49±0.33 KJ mol^{-1} and ΔS of 66±2 J mol^{-1} K^{-1}. Based on the values of ΔG, ΔH, and ΔS, it can be inferred that electrostatic interaction serves as the main driving force behind the LF-RD complex formation (Zheng et al., 2020).

Infrared spectrum analysis

FTIR analysis was conducted to enhance the comprehension of the chemical structures of LF and RD, along with their chemical interactions in complex coacervation. Based on the findings presented in Fig. 3A, the LF spectrum displayed several characteristic peaks indicative of the protein structure. Notably, the peak at 3,280 cm^{-1} signified the presence of O–H groups in free amino acids, whereas the band observed at 2,931 cm^{-1} linked to the stretching vibration of C–H. Furthermore, the peaks found at 1,635, 1,516, and 1,390 cm^{-1} are associated with Amide I (stretching of CO and CN), Amide II (primarily bending of NH), and Amide III (stretching of CN), respectively (Bastos et al., 2018). For the RD spectrum, the peaks at 3,305 cm^{-1} and 2,922 cm^{-1} are characteristic absorption bands connected with O–H and C–H in polysaccharides, respectively (Qiu et al., 2022). Another band detected at 1,010 cm^{-1} was linked to the structure of saccharide (C–O–C; Yang et al., 2021). The asymmetric and symmetric stretching vibrations of the carboxylic group were exhibited as two peaks at 1,644 and 1,421 cm^{-1} (Chen et al., 2022).

The spectrum of the LF-RD coacervates demonstrated a combination of characteristic peaks from LF and RD, even though with slight shifts compared to LF and RD individually. Specifically, the absorption bands at 1,644 and 1,421 cm^{-1}, typical of RD molecules, disappeared in the LF-RD coacervate spectrum. Additionally, the peaks corresponding to Amide I (1,650 cm^{-1}) and Amide II (1,545 cm^{-1}) in LF-RD coacervate displayed shifts relative to those in LF (1,635 and 1,516 cm^{-1}), indicating the occurrence of electrostatic interaction between the amino group of LF and the carboxylic group of RD (Constantino and Garcia-Rojas, 2023). Moreover, the band in LF at 3,280 cm^{-1} shifted to 3,313 cm^{-1} in LF-RD coacervate,

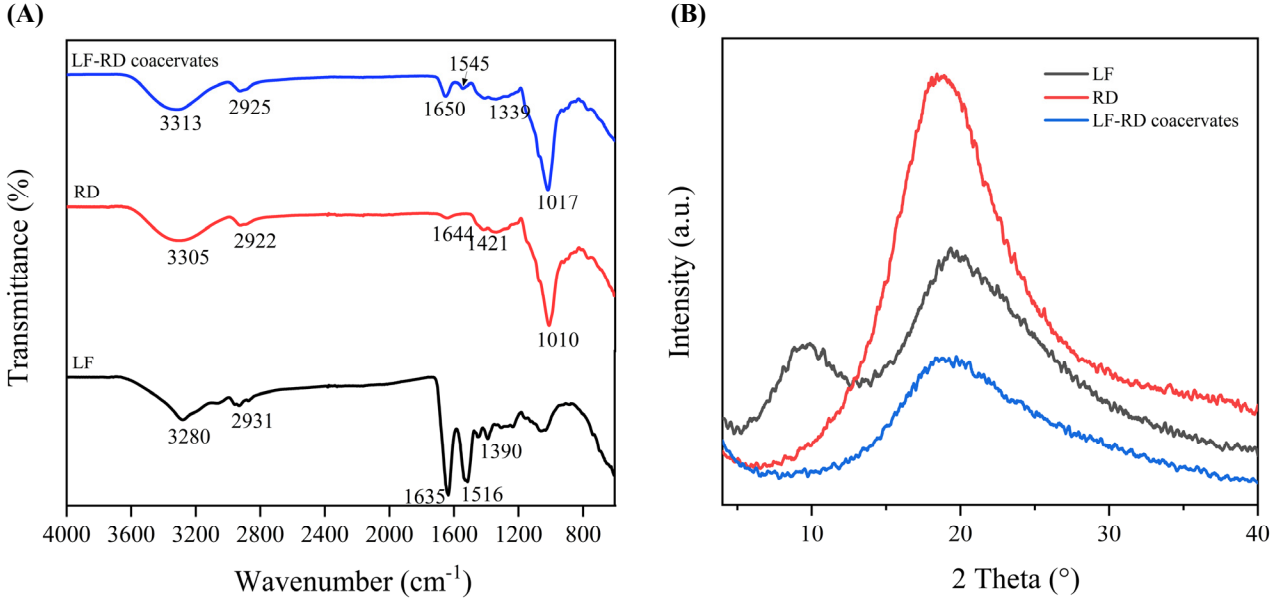

Fig. 3. Structural characterization of LF, RD, and LF-RD complex coacervates by (A) FTIR spectra and (B) X-ray diffractogram. LF, lactoferrin; RD, resistant dextrin; FTIR, Fourier transform infrared.

suggesting the formation of a hydrogen bond (Sun et al., 2017). It is noteworthy that no new peaks emerged, signifying the absence of chemical bonds or chemical groups. Based on all of the findings from the FTIR analysis, it can be concluded that hydrogen bonding, in addition to electrostatic interactions, significantly contributes to the formation of complex coacervates.

X-ray diffractogram analysis

X-ray diffraction was utilized to assess the crystallinity level and differentiate between amorphous and crystalline properties. The presence of sharp peaks in the X-ray diffractogram (XRD) indicated a crystalline arrangement, whereas broad peaks suggested an amorphous structure. As illustrated in Fig. 3B, LF exhibited two flat crystal peaks at diffraction angles 2θ of 9.9° and 19.3°, suggesting the protein's amorphous characteristics. On the other hand, the RD diffractogram displayed a prominent peak at 19.2° (2θ), potentially enhancing electrostatic interactions owing to the existence of covalent bonds (Hasanvand and Rafe, 2018). Nevertheless, in the XRD curve of the LF-RD complex, the characteristic crystallization peak of LF at 9.9° nearly vanished, displaying a considerably reduced peak intensity compared to LF and RD individually. This suggests a transition of the molecular structure of the complex to a more amorphous state. Presumably, the LF molecule chains were closely absorbed by the RD molecules, resulting in the formation of an amorphous complex between LF and RD by intermolecular interaction (electrostatic attraction and hydrogen bonding). The XRD findings were in agreement with the FTIR data in this study, and similar conclusions have been documented by Li et al. (2021b).

Morphological characteristics of the complex coacervates

The surface morphology of LF, RD, and LF-RD complex coacervates was visualized using SEM. As shown in Fig. 4A, the LF exhibited a smooth lamellar structure without any visible cracks on the surface. A comparison with LF-RD complex coacervates (Fig. 4C, red circles) revealed that the sheet-like structure of LF was thinner than that of the LF-RD complex coacervates. Moreover, the surface of LF-RD complex coacervate displays a porous texture, which is attributed to the ice crystals or bubbles evaporating during the freezing process. These pores on the surface act as conduits facilitating the diffusion of oxygen from the atmosphere into the interior of the particle (Xiao and Ahn, 2023). Meanwhile, Figs. 4D and E shows that the surface of the coacervate showcases a concave spherical morphology resembling RD particles (yellow circles), accompanied by distinct three-dimensional (3D) spatial arrangements (blue circles). It is postulated that the unique 3D microstructure contributes to the improved thermal stability observed in the LF-RD coacervate formation. These observations provide further evidence of strong interactions between LF and RD.

Using the label distribution of fluorescent colors, CLSM was employed to further analyze the microstructure of the LF-RD complex coacervates. Figs. 4F, G, and H shows the fluorescence images of the LF-RD complex observed at different emission wavelengths. Specifically, Fig. 5F shows Nile blue-labeled LF emitting green fluorescence, Fig. 4G displays 5-aminofluorescein-labeled RD emitting red fluorescence, and Fig. 5H presents LF-RD complexes under the effect of the two fluorescent dyes. The yellow fluorescence appearing in the field of view is attributed to RD being wrapped around the surface of aggregated LF through electrostatic and hydrogen bonding interactions, resulting in a core-shell structure with LF as the core and RD as the shell. At higher concentration of LF-RD complex solution (1%, w/v), both LF and RD underwent a large area of agglomeration, revealing a pronounced formation of a tight and continuous membrane by RD, completely enveloping LF within it (Figs. 4I, J, and K). These CLSM images validate the inferences drawn from the XRD curves. Consequently, on the basis of the aforementioned findings, it can be inferred that the LF-RD complex was effectively synthesized.

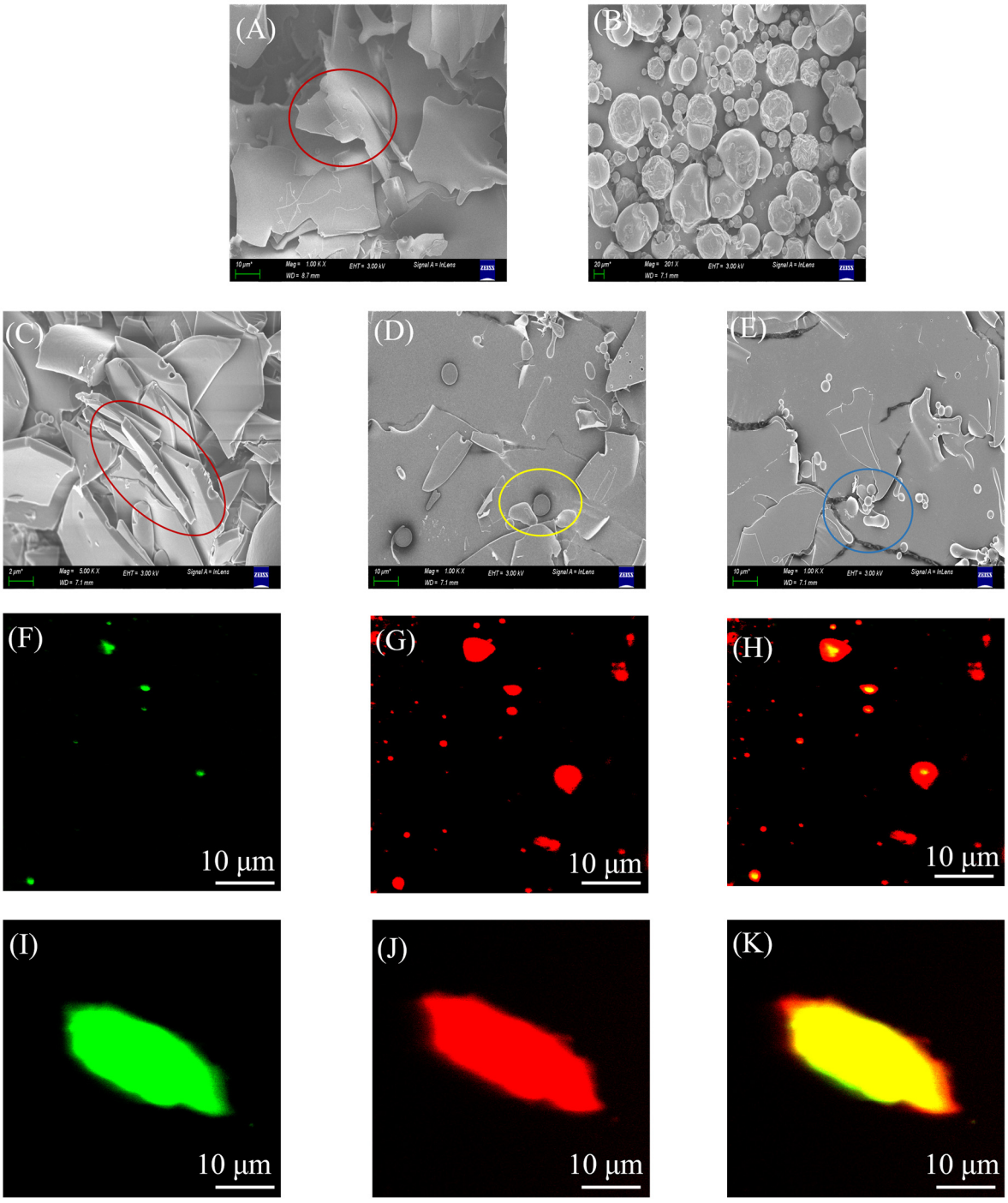

Fig. 4. Observation of the microstructure of LF, RD and LF-RD complex coacervates. Scanning electron microscopic images of (A) LF observed at ×1,000; (B) RD observed at ×201; (C–E) LF-RD complex (pH 7.0, LF/RD 1:12) observed at ×5,000, ×1,000 [(D,E) under different fields of view], respectively. (F–K) Confocal laser scanning microscopic images of LF-RD complexes at different concentrations (0.01% and 1% w/v, respectively). LF was stained with Nile blue as a green color, and RD was stained with 5-aminofluorescein as a red color. LF, lactoferrin; RD, resistant dextrin.

8-Anilino-1-naphthalenesulfonic acid fluorescence spectrum

The surface hydrophobicity of LF exhibited a corresponding increase with rising concentration of RD, as illustrated in Fig. 5A. This observation can be attributed to the electrostatic complexation that occurs between LF and RD upon the introduction

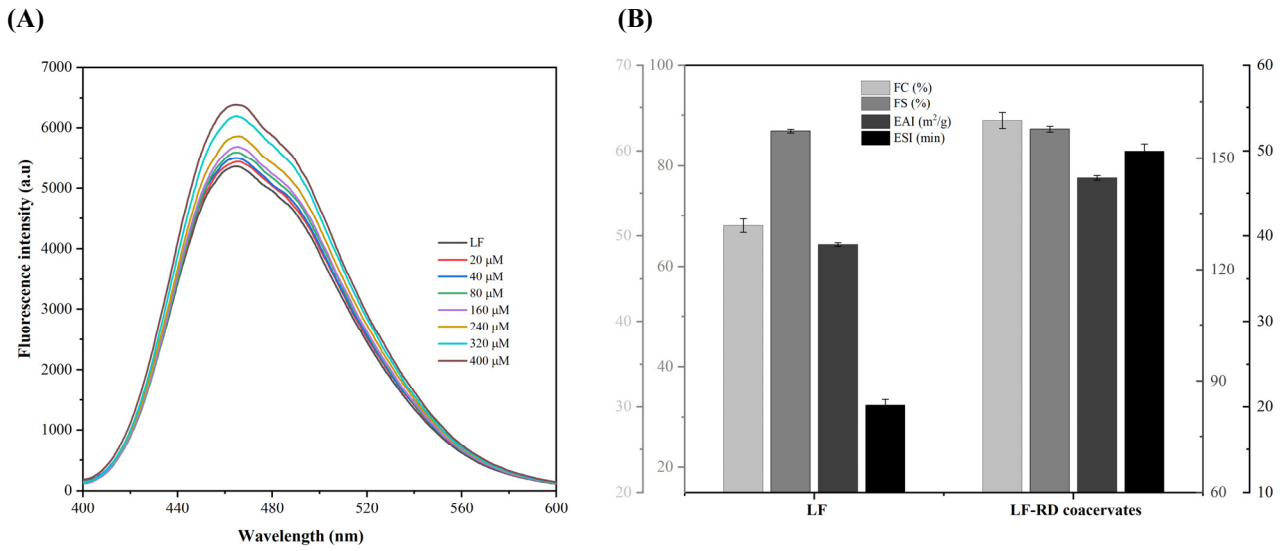

Fig. 5. Characterization of ANS fluorescence and functional properties in LF and LF-RD complex coacervates. (A) Changes in ANS fluorescence intensity of LF (12.5 μM) with different RD concentrations. (B) Foaming and emulsification properties of LF and LF-RD complex coacervates. LF, lactoferrin; FC, foam capacity; FS, foam stability; EAI, emulsion activity index; ESI, emulsification stability index; RD, resistant dextrin; ANS, 8-anilino-1-naphthalenesulfonic acid.

of RD, which facilitates the unfolding of LF molecules and the subsequent exposure of their hydrophobic regions. This exposure facilitates the occurrence of hydrophobic interactions. With increasing RD concentration, complexation became stronger, resulting in greater exposure of the hydrophobic regions and consequently stronger hydrophobic interactions, ultimately facilitating the formation of protein aggregates. This observation aligns with the findings obtained from the turbidity measurements. Moreover, during this process, LF exhibits a positive zeta potential, whereas ANS acts as an anion that can electrostatically interact with LF, thereby contributing to an elevated hydrophobicity. The schematic model for the interaction of LF and RD has been shown in Fig. 6. Naderi et al. (2020) similarly observed that the surface hydrophobicity of the complex formed by oak protein isolate and gum arabic was greater than that of the oak protein isolate solution.

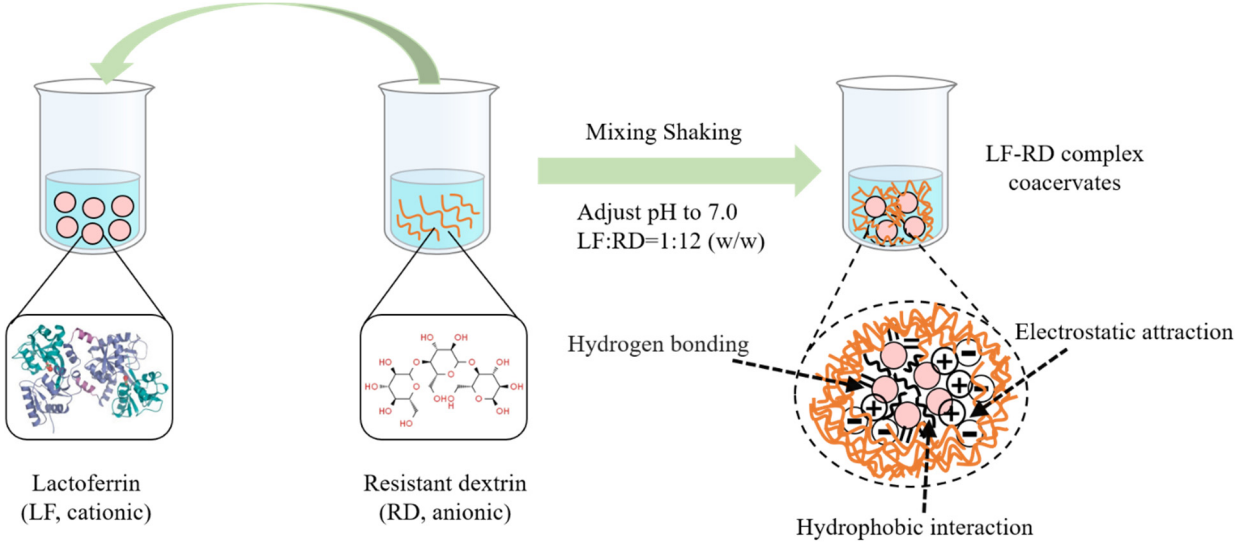

Fig. 6. Schematic model for the interaction of LF and RD. The structure of LF from Baker and Baker (2005).

Foaming and emulsification properties

The foaming properties of LF-RD complex coacervates were studied by preparing LF foams before and after combined with RD, and recording their appearance data. The findings presented in Fig. 5B demonstrate that the addition of RD notably enhanced both the foam ability and foam stability in comparison to LF alone. Specifically, the foam ability of LF increased from 51.2% to 63.5% upon incorporation of RD, representing an increase of 12.3%. The enhancement of LF foaming may be attributed to the rapid conformational alterations and rearrangement of LF at the air-water interface post-compounding with RD (Razi et al., 2019). This process results in the formation of a viscoelastic film through intermolecular interactions, enhancing the stability of the interface layer (Dickinson, 2011). Furthermore, the enhanced stability of the foam was linked to the interactions of proteins and polysaccharides, which could enhance the stability of the interfacial layer, resulting in a more stable foam to prevent bubble coalescence (He et al., 2021). Compared to the findings of Yan et al. (2022), the improvement of foaming properties was observed in this study following LF coacervation with RD. This finding is of great significance for promoting the development of all-natural functional foaming agents.

Similarly, the impact of RD on the emulsifying properties of LF was further analyzed. Fig. 5B shows that upon interaction with RD, the EAI and ESI of LF increased by around 14.1% and 147.0%, respectively. These notable enhancements in the emulsification properties stand in contrast to the findings of Li et al. (2021c), which indicated that the coacervation of hyaluronic acid with LF did not lead to a substantial enhancement in the emulsification properties (EAI and ESI) of LF. Zhu et al. (2017) pointed out that surface hydrophobicity is positively correlated with the EAI and ESI, aligning with the emulsification findings presented in this research. Data from external fluorescence spectroscopy indicated an increase in the hydrophobicity of LF with the addition of RD. Consequently, increasing the protein's surface hydrophobicity is advantageous for enhancing its emulsification index. As reported by He et al. (2021), the mechanism of stable emulsion by polysaccharides involves two main aspects. Firstly, polysaccharides have the capability to attach to the droplet's surface, forming a protective barrier that aids in stabilizing the oil droplet by means of steric hindrance. Secondly, polysaccharides may create a dense and substantial interface layer encasing the oil droplet, which not only enhances dimensional stability but also helps prevent protein aggregation and flocculation.

Thermal stability analysis

DSC thermograms were employed to analyze the thermal stability of the LF, RD, and LF-RD coacervates. As depicted in Fig. 7A, the RD thermogram revealed an endothermic peak at 94.99℃ as a result of the free water release from the RD powder. In contrast, the DSC curve of LF displayed a wide endothermic peak at 85.57°C, which was attributed to the denaturation of LF. The thermal denaturation of LF is known to be affected by various environmental factors, including pH, ionic strength, and conformational state (Native, Holo, and Apo; Santos et al., 2021). In the complex coacervate, the first peak at 72.14℃ was attributed to the evaporation of free water from the sample matrix, whereas the second peak at 154.43℃ was related to the denaturation of the complex coacervates. The increased temperature for denaturation noted in the complex coacervates might result from the electrostatic interactions and hydrogen bonds between LF and RD, contributing to a more stable network structure (Dong et al., 2023). This discovery aligns with previous reports that complex coacervation with polysaccharides can enhance the thermal stability of proteins (Li et al., 2024, Lin et al., 2022).

The TGA and derivative thermogravimetric curves presented in Figs. 7B and C delineated a two-stage decomposition process occurring within the temperature range of 30℃–600℃. The initial stage, spanning 30℃–150℃, was characterized by weight loss attributed to the discharge of remaining moisture within the samples. Subsequently, a significant and rapid

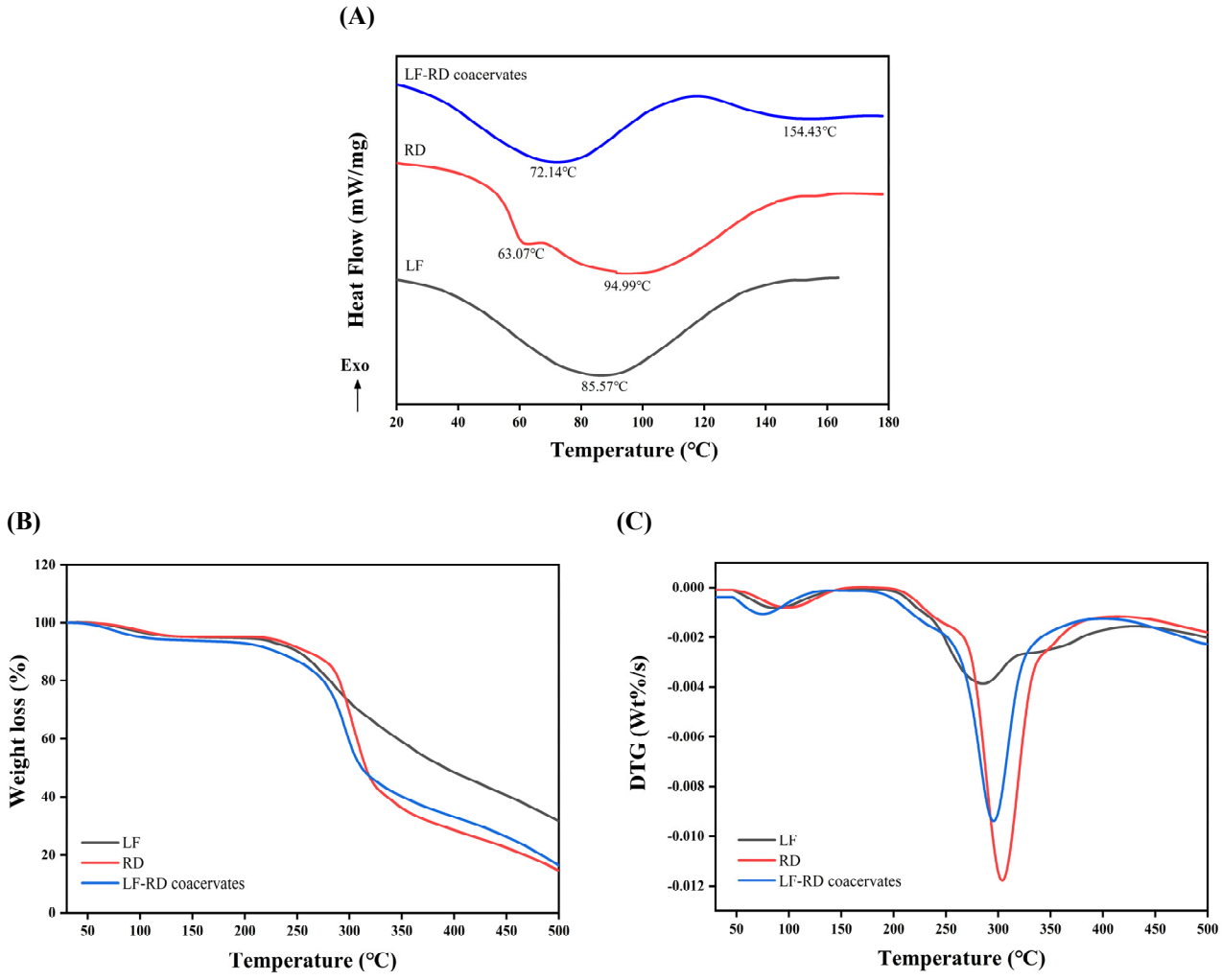

Fig. 7. Thermal analysis of LF, RD, and LF-RD complex coacervates by (A) DSC thermograms, (B) TGA, and (C) DTG curves. LF, lactoferrin; RD, resistant dextrin; DTG, derivative thermogravimetric; DSC, differential scanning calorimetry; TGA, thermogravimetric.

weight loss was observed in the subsequent phase, commencing at approximately 200°C, indicating the breakdown of samples. The degradation of the coacervate is primarily attributed to the decomposition of LF and RD. In the case of LF, degradation occurs through the breakdown of non-covalent electrostatic bonds and hydrophobic interactions, followed by the disruption of the covalent bonds of amino acid residues with increasing temperature (Li et al., 2020). In addition, the temperature corresponds to the maximum weight loss rate (Tmax) that occurs for the LF and LF-RD complexes are 285°C and 296°C, respectively. The Tmax of the complex surpasses that of LF alone, aligning with the findings from the DSC analysis. Therefore, the LF-RD complex coacervate exhibits potential for encapsulating a wide range of heat-sensitive compounds including fragrances, essential oils, and bioactive compounds.

Antioxidant activity

The antioxidant activity of LF can be attributed to the presence of sulfhydryl groups in its amino acid composition, particularly methionine and cysteine, which function as antioxidants through reduction reactions (Elias et al., 2008). As shown in Fig. 8A, the DPPH radical scavenging activities of GA, used as a standard control, exhibit a substantial capacity for radical scavenging. It is important to highlight that the DPPH scavenging activity of LF was observed to a significantly

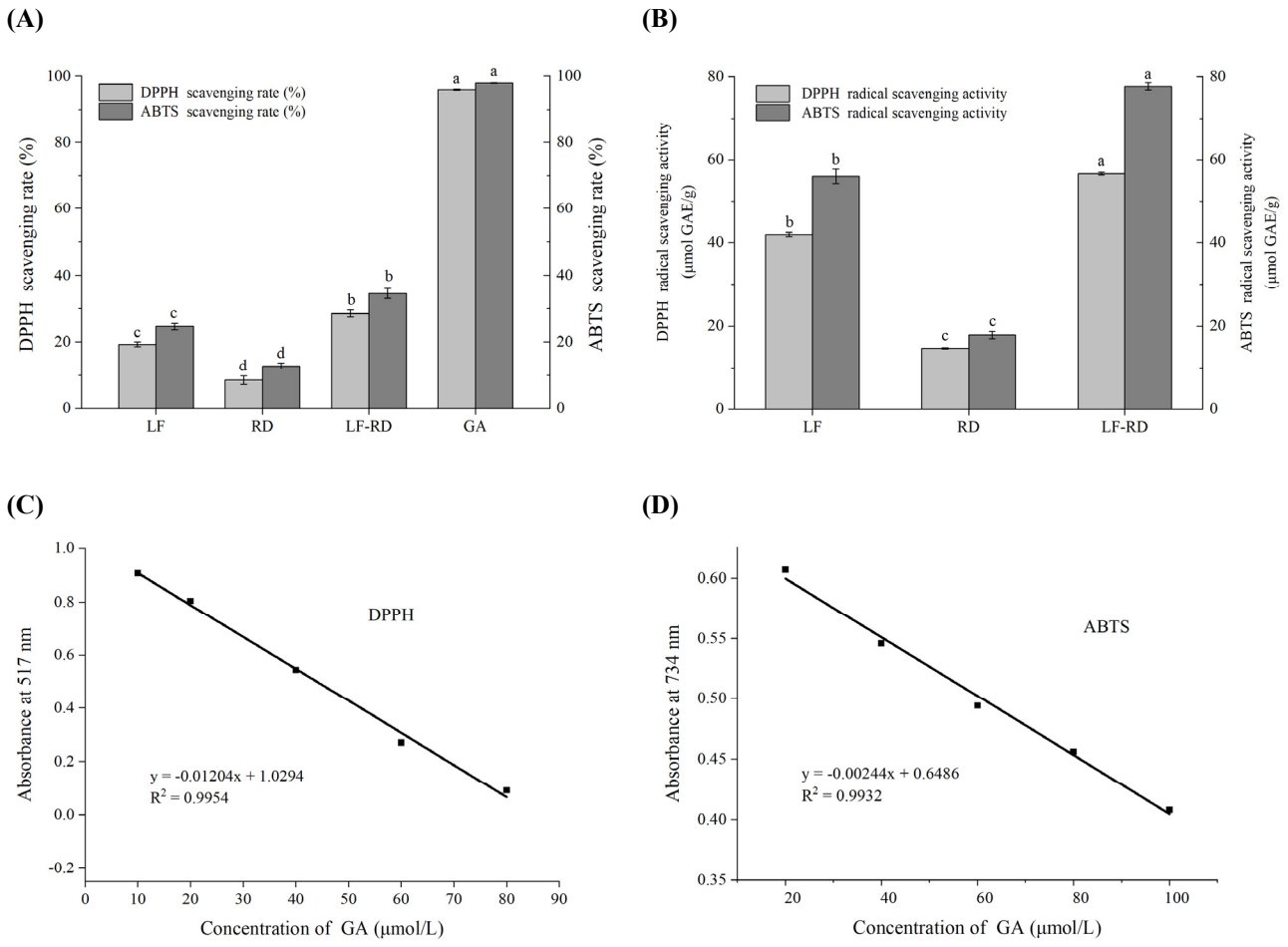

Fig. 8. Antioxidant activity assays of LF, RD and LF-RD complex coacervates. (A) DPPH and ABTS scavenging rate; (B) DPPH and ABTS radical scavenging activity; (C) Standard curve of gallic acid scavenging DPPH free radicals; (D) Standard curve of gallic acid scavenging ABTS free radicals. GA represents gallic acid and GAE represents gallic acid equivalent. $^{a–d}$ Different letters represent significant differences among the LF, RD, LF-RD and GA ($p<0.05$). DPPH, 2, 2-diphenyl-1-picrylhydrazyl; ABTS, 2,2'-azino-bis(3-ethylbenzothiazoline-6-sulfonic acid); LF, lactoferrin; RD, resistant dextrin; GA, gallic acid; GAE, gallic acid equivalent.

enhanced following coacervation with RD, indicating a potential synergistic effect between LF and RD. This synergistic interaction may facilitate the unfolding of the LF molecular structure, thereby exposing more hydrophobic groups that can interact with fat-soluble DPPH free radicals, ultimately improving its scavenging capacity (He et al., 2023). Furthermore, the complex coacervation of LF with RD introduced additional hydroxyl groups, which are conducive to terminating free radical chain reactions, thereby imparting the LF-RD complex with enhanced free radical scavenging activity. In alignment with the findings related to DPPH, the ABTS free radical scavenging rate of LF was recorded at 24.68±0.95%, whereas its radical scavenging capacity increased to 34.51±1.44% after complexation with RD, representing an enhancement of 39.8% (Fig. 8A). Furthermore, GAE was employed to estimate the antioxidant activity of the LF-RD complex coacervates. As depicted in Figs. 8C and D, a strong linear relationship was observed between the concentration of the GA standard and its absorbance. Within the examined concentration range, the linear regression equation for the DPPH assay is $y=–0.01204x+1.0294$ ($r^2=0.9954$), and for the ABTS assay, it is $y=–0.00244x+0.6486$ ($r^2=0.9932$). Consequently, the DPPH and ABTS free radical scavenging capacities of the samples can be quantified as GAE using the standard curve, thereby providing an indication of their antioxidant activity. As shown in Fig. 8B, LF exhibited a notable enhancement in antioxidant activity following

complexation with RD, demonstrating a 35.9% increase in DPPH radical scavenging activity and a 38.7% increase in ABTS radical scavenging activity. And a similar trend is observed with the DPPH and ABTS scavenging rate in Fig. 8A. These findings indicate that the complex coacervates formed by the combination of LF and RD may function as effective carriers for the encapsulated delivery of unstable bioactive ingredients, such as omega-3, 6 fatty acids or curcumin.

In vitro digestive properties of lactoferrin and lactoferrin-resistant dextrin complex coacervates in infants and young children

Fig. 9 illustrates the degradation patterns of LF and LF-RD complex coacervates during the gastric digestion phase. LF displayed a prominent band at around 80 kDa, while the band after LF complexed with RD showed a slight upward shift, indicating the formation of higher molecular weight complexes. Notably, after 30 min of gastric digestion, the complexes formed by LF and RD maintained intact LF bands (red dashed box), suggesting a degree of resistance to pepsin hydrolysis. This resistance may be attributed to the encapsulation of LF by certain RD molecules, which could partially shield the active sites of gastric proteases, thereby enhancing LF's resistance to protein hydrolysis. However, this protective effect appeared to diminish over time, with the LF-RD complex coacervates eventually degrading similarly to LF alone. Similar findings by David-Birman et al. (2013) demonstrated that HMP-coated LF particles did not protect LF from immediate pepsin digestion, whereas LMP-coated LF particles still exhibited a complete LF signature band after 10 min of pepsin digestion. And, beyond this duration, no LF signature band was detectable, which is consistent with the results observed in the current study. Overall, the coacervation

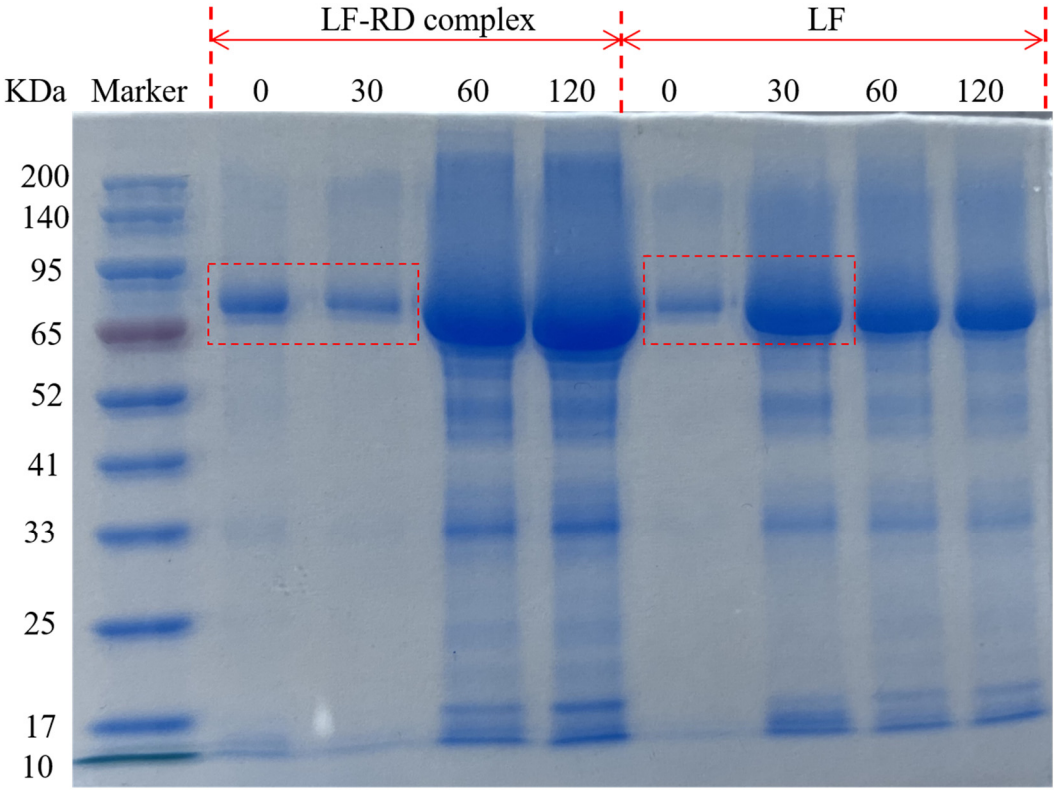

Fig. 9. SDS-PAGE analysis of LF and LF-RD complex coacervates using an *in vitro* infant gastric simulated digestion. The numbers 0, 30, 60, and 120 correspond to the time points (min) following the initiation. LF, lactoferrin; RD, resistant dextrin; SDS-PAGE, sodium dodecyl sulfate-polyacrylamide gel electrophoresis.

process involving LF and RD is expected to regulate the digestion rate of LF. This mechanism may prove to be a viable approach for managing LF digestion, thereby facilitating the delivery of intact LF to the upper gastrointestinal tract.

Microstructure and encapsulation rate of docosahexaenoic acid microcapsules

Optical microscopy images of DHA microcapsules encapsulation process are presented in Figs. 10A, B, anc C, with red circles indicating the presence of oil droplets. Following the emulsification process (Fig. 10A), numerous spherical particles characterized by well-defined walls and a singular core were observed. However, some of the LF-DHA droplets exhibited aggregation, resulting in irregular shapes. After complex coacervation, a denser wall formed around the oil droplets, attributable to the interaction between RD and LF. Concurrently, the droplets were uniformly dispersed within the emulsions, adopting a completely spherical shape. Notably, the size of the emulsion post-complex coacervation was marginally larger than that of LF-DHA, indicating a successful integration of LF and RD. This observation is consistent with previously obtained particle size results. Moreover, the presence of transglutaminase facilitates a tighter binding of the condensates through the cross-linking of LF, resulting in the formation of a denser wall around the oil droplets (as shown in Fig. 10C).

The fluorescence micrograph of DHA microcapsules is depicted in Figs. 10D, E, and F. Where the aqueous protein phase was shown in green and the oil phase was shown in red in the figure. It is evident that the DHA microcapsules were well dispersed in the emulsion without significant aggregation. The microstructural analysis revealed an inner oil phase encased by

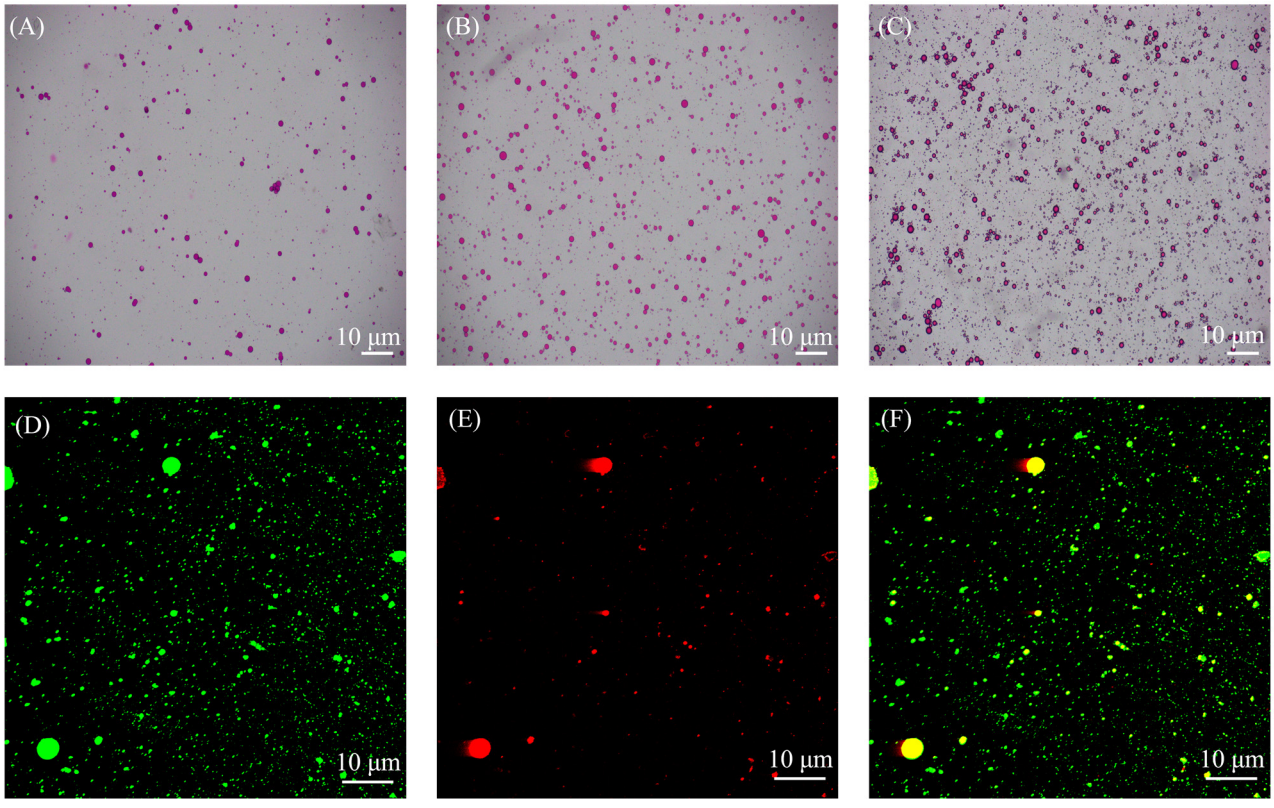

Fig. 10. Microscopic observation during the microencapsulation process of DHA. Optical microscopy of the DHA microencapsulation process with Nile red dye: (A) LF-DHA emulsion (×400), (B) LF-RD-DHA emulsion (×400), and (C) DHA microcapsules after transglutaminase crosslinking (×400). The white bars represent 1 μm in scale. Confocal laser scanning microscopy images of DHA microcapsules: (D) protein stained with Nile blue, (E) DHA stained with Nile red, and (F) a combined image of DHA microcapsules in the presence of two fluorescent stains. DHA, docosahexaenoic acid; LF, lactoferrin; RD, resistant dextrin.

an outer protein phase, indicating that the LF-RD complex coacervates effectively functions as a carrier for the successful encapsulation of DHA. With favorable morphological characteristics, DHA microcapsules also demonstrated a notable encapsulation efficiency of 89±3.4%, surpassing the encapsulation efficiency of black pepper essential oil within LF-sodium alginate complex coacervates as reported by Bastos et al. (2020). Jensen et al. (2005) reported that maternal supplementation with DHA during pregnancy, breastfeeding, or the consumption of DHA-enriched formula can elevate DHA levels in infants, thereby facilitating improved visual and cognitive development. Consequently, the findings presented in this study hold considerable importance.

Conclusion

This study demonstrated that LF can form complex coacervates with RD, thereby enhancing the thermal stability and functional properties of LF, including its foaming and emulsifying capacities. It was observed that both the LF to RD ratio and pH significantly influenced the extent of coacervation. Notably, at a pH of 7.0 and an LF:RD ratio of 1:12, the LF-RD complex coacervate achieved a zeta potential close to zero, displaying maximum turbidity, particle size, and coacervate yield. Moreover, the binding process of LF and RD involved an increase in the hydrophobicity of the LF surface and a modification of LF conformation. The negative ΔG values suggested that the binding of LF to RD was spontaneous and thermodynamically favorable. In addition to electrostatic complexation, the formation of LF-RD complex coacervates was also facilitated by hydrophobic interactions and hydrogen bonding. Furthermore, following complex coacervation with RD, LF exhibited superior thermal stability, antioxidant properties, stability in the gastric environment, as well as improved foaming and emulsifying properties. Microscopic analysis of the LF-RD coacervate revealed distinct 3D spatial structures, with fluorescence co-localization confirming the formation of a complete core-shell architecture. Results from optical microscopy and CLSM showed that the LF-RD complex effectively encapsulated DHA. This study provides a theoretical framework for the potential application of microencapsulated DHA utilizing LF-RD complex coacervates in infant formula.

Conflicts of Interest

The authors declare no potential conflicts of interest.

Acknowledgements

This work was supported by the Shandong Province small and medium-sized scientific and technological enterprises innovation capacity improvement project (No.2025TSGCCZZB0777), Natural Science Foundation of Shandong Province (ZR2023QC111, ZR2024MC145).

Author Contributions

Conceptualization: Wang C, Zhang X. Data curation: Luo J, Li H, Wan J. Formal analysis: Wang N, Zhao Y, Wang C, Zhang X. Methodology: Luo J, Wang C, Zhang X. Software: Luo J, Zhang X. Validation: Li H, Wan J, Zhao Y. Investigation: Wang N, Jiang H, Wang C. Writing - original draft: Luo J. Writing - review & editing: Luo J, Wang N, Li H, Wan J, Zhao Y, Jiang H, Wang C, Zhang X.

Ethics Approval

This article does not require IRB/IACUC approval because there are no human and animal participants.

References

Ahad T, Gull A, Masoodi FA, Gani A, Nissar J, Ganaie TA, Masoodi L. 2023. Protein and polysaccharide based encapsulation of ginger oleoresin: Impact of wall materials on powder stability, release rate and antimicrobial characteristics. Int J Biol Macromol 240:124331.

Baker EN, Baker HM. 2005. Molecular structure, binding properties and dynamics of lactoferrin. Cell Mol Life Sci 62:2531-2539.

Bastos LPH, de Carvalho CWP, Garcia-Rojas EE. 2018. Formation and characterization of the complex coacervates obtained between lactoferrin and sodium alginate. Int J Biol Macromol 120:332-338.

Bastos LPH, Dos Santos CHC, de Carvalho MG, Garcia-Rojas EE. 2020. Encapsulation of the black pepper (*Piper nigrum* L.) essential oil by lactoferrin-sodium alginate complex coacervates: Structural characterization and simulated gastrointestinal conditions. Food Chem 316:126345.

Chen K, Zhang M, Adhikari B, Wang M. 2022. Microencapsulation of Sichuan pepper essential oil in soybean protein isolate-Sichuan pepper seed soluble dietary fiber complex coacervates. Food Hydrocoll 125:107421.

Chen K, Zhang M, Mujumdar AS, Wang H. 2021. Quinoa protein-gum Arabic complex coacervates as a novel carrier for eugenol: Preparation, characterization and application for minced pork preservation. Food Hydrocoll 120:106915.

Chen W, Wang H, Zhang K, Gao F, Chen S, Li D. 2016. Physicochemical properties and storage stability of microencapsulated DHA-rich oil with different wall materials. Appl Biochem Biotechnol 179:1129-1142.

Constantino ABT, Garcia-Rojas EE. 2023. Microencapsulation of beta-carotene by complex coacervation using amaranth carboxymethyl starch and lactoferrin for application in gummy candies. Food Hydrocoll 139:108488.

David-Birman T, Mackie A, Lesmes U. 2013. Impact of dietary fibers on the properties and proteolytic digestibility of lactoferrin nano-particles. Food Hydrocoll 31:33-41.

Dickinson E. 2011. Mixed biopolymers at interfaces: Competitive adsorption and multilayer structures. Food Hydrocoll 25:1966-1983.

Dong S, Hu SM, Yu SJ, Zhou S, Zhou T. 2023. Soybean protein isolate/chitosan complex-rutin microcapsules. Int J Biol Macromol 243:125323.

El Ghazzaqui Barbosa A, Constantino ABT, Bastos LPH, Garcia-Rojas EE. 2022. Encapsulation of sacha inchi oil in complex coacervates formed by carboxymethylcellulose and lactoferrin for controlled release of β-carotene. Food Hydrocoll Health 2:100047.

Elias RJ, Kellerby SS, Decker EA. 2008. Antioxidant activity of proteins and peptides. Crit Rev Food Sci Nutr 48:430-441.

Fu J, Song L, Liu Y, Bai C, Zhou D, Zhu B, Wang T. 2020. Improving oxidative stability and release behavior of docosahexaenoic acid algae oil by microencapsulation. J Sci Food Agric 100:2774-2781.

Hao L, Shan Q, Wei J, Ma F, Sun P. 2019. Lactoferrin: Major physiological functions and applications. Curr Protein Pept Sci 20:139-144.

Hasanvand E, Rafe A. 2018. Characterization of flaxseed gum/rice bran protein complex coacervates. Food Biophys 13:387-395.

He JL, Liu BH, Zhang HL, Xu D, Shi BM, Zhang YH. 2023. Improvement of hydrolysis efficiency and interfacial properties of zein using nanoemulsions prepared by a low energy emulsification method. Food Biosci 54:102922.

He W, Xiao N, Zhao Y, Yao Y, Xu M, Du H, Wu N, Tu Y. 2021. Effect of polysaccharides on the functional properties of egg white protein: A review. J Food Sci 86:656-666.

Jensen CL, Voigt RG, Prager TC, Zou YL, Fraley JK, Rozelle JC, Turcich MR, Llorente AM, Anderson RE, Heird WC. 2005. Effects of maternal docosahexaenoic acid intake on visual function and neurodevelopment in breastfed term infants. Am J Clin Nutr 82:125-132.

Krzeminski A, Prell KA, Busch-Stockfisch M, Weiss J, Hinrichs J. 2014. Whey protein–pectin complexes as new texturising elements in fat-reduced yoghurt systems. Int Dairy J 36:118-127.

Li D, Zhu L, Wu Q, Chen Y, Wu G, Zhang H. 2023. Different interactions between Tartary buckwheat protein and Tartary buckwheat phenols during extraction: Alterations in the conformation and antioxidant activity of protein. Food Chem 418:135711.

Li F, Wang H, Mei X. 2021a. Preparation and characterization of phytosterol-loaded microcapsules based on the complex coacervation. J Food Eng 311:110728.

Li L, Lai B, Yan JN, Yambazi MH, Wang C, Wu HT. 2024. Characterization of complex coacervation between chia seed gum and whey protein isolate: Effect of pH, protein/polysaccharide mass ratio and ionic strength. Food Hydrocoll 148:109445.

Li M, Li X, McClements DJ, Shi M, Shang Q, Liu X, Liu F. 2021b. Physicochemical and functional properties of lactoferrin-hyaluronic acid complexes: Effect of non-covalent and covalent interactions. LWT-Food Sci Technol 151:112121.

Li Q, Lan H, Zhao Z. 2019. Protection effect of sodium alginate against heat-induced structural changes of lactoferrin molecules at neutral pH. LWT-Food Sci Technol 99:513-518.

Li Q, Zhao Z. 2017. Formation of lactoferrin/sodium caseinate complexes and their adsorption behaviour at the air/water interface. Food Chem 232:697-703.

Li T, Hu P, Dai T, Li P, Ye X, Chen J, Liu C. 2018. Comparing the binding interaction between *β*-lactoglobulin and flavonoids with different structure by multi-spectroscopy analysis and molecular docking. Spectrochim Acta A Mol Biomol Spectrosc 201:197-206.

Li X, Li M, Zhang T, McClements DJ, Liu X, Wu X, Liu F. 2021c. Enzymatic and nonenzymatic conjugates of lactoferrin and (−)-epigallocatechin gallate: Formation, structure, functionality, and allergenicity. J Agric Food Chem 69:6291-6302.

Li Z, Ma D, He Y, Guo S, Liu F, Liu X. 2020. Simultaneous ultrasound and heat enhance functional properties of glycosylated lactoferrin. Molecules 25:5774.

Lin T, Dadmohammadi Y, Davachi SM, Torabi H, Li P, Pomon B, Meletharayil G, Kapoor R, Abbaspourrad A. 2022. Improvement of lactoferrin thermal stability by complex coacervation using soy soluble polysaccharides. Food Hydrocoll 131:107736.

Liu S, Low NH, Nickerson MT. 2009. Effect of pH, salt, and biopolymer ratio on the formation of pea protein isolate−gum arabic complexes. J Agric Food Chem 57:1521-1526.

Ménard O, Bourlieu C, De Oliveira SC, Dellarosa N, Laghi L, Carrière F, Capozzi F, Dupont D, Deglaire A. 2018. A first step towards a consensus static *in vitro* model for simulating full-term infant digestion. Food Chem 240:338-345.

Meng Q, Jiang H, Tu J, He Y, Zhou Z, Wang R, Jin W, Han J, Liu W. 2024. Effect of pH, protein/polysaccharide ratio and preparation method on the stability of lactoferrin-polysaccharide complexes. Food Chem 456:140056.

Ministry of Health of the People's Republic of China. 2020. GB/T 39100-2020: Determination of antioxidant activity for

polypeptides: DPPH and ABTS methods. Ministry of Health of the People's Republic of China, Beijing, China.

Naderi B, Keramat J, Nasirpour A, Aminifar M. 2020. Complex coacervation between oak protein isolate and gum Arabic: Optimization & functional characterization. Int J Food Prop 23:1854-1873.

Peinado I, Lesmes U, Andrés A, McClements JD. 2010. Fabrication and morphological characterization of biopolymer particles formed by electrostatic complexation of heat treated lactoferrin and anionic polysaccharides. Langmuir 26:9827-9834.

Qiu L, Zhang M, Adhikari B, Chang L. 2022. Microencapsulation of rose essential oil in mung bean protein isolate-apricot peel pectin complex coacervates and characterization of microcapsules. Food Hydrocoll 124:107366.

Razi SM, Motamedzadegan A, Shahidi SA, Rashidinejad A. 2019. Physical and rheological properties of egg albumin foams are affected by ionic strength and basil seed gum supplementation. Int J Chem Eng 2019:2502908.

Rossi AM, Taylor CW. 2011. Analysis of protein-ligand interactions by fluorescence polarization. Nat Protoc 6:365-387.

Samanta R, Ganesan V. 2018. Influence of protein charge patches on the structure of protein–polyelectrolyte complexes. Soft Matter 14:9475-9488.

Santos MB, Geraldo de Carvalho M, Garcia-Rojas EE. 2021. Carboxymethyl tara gum-lactoferrin complex coacervates as carriers for vitamin D3: Encapsulation and controlled release. Food Hydrocoll 112:106347.

Sun C, Dai L, Gao Y. 2017. Formation and characterization of the binary complex between zein and propylene glycol alginate at neutral pH. Food Hydrocoll 64:36-47.

Tian L, Roos YH, Miao S. 2023. Phase behavior and complex coacervation of whey protein isolate-*Tremella fuciformis* polysaccharide solution. Food Hydrocoll 143:108871.

Tokle T, Lesmes U, McClements DJ. 2010. Impact of electrostatic deposition of anionic polysaccharides on the stability of oil droplets coated by lactoferrin. J Agric Food Chem 58:9825-9832.

Tomé Constantino AB, Garcia-Rojas EE. 2022. Vitamin D_3 microcapsules formed by heteroprotein complexes obtained from amaranth protein isolates and lactoferrin: Formation, characterization, and bread fortification. Food Hydrocoll 129:107636.

Trithavisup K, Krusong K, Tananuwong K. 2019. In-depth study of the changes in properties and molecular structure of cassava starch during resistant dextrin preparation. Food Chem 297:124996.

Wang Y, Ye A, Hou Y, Jin Y, Xu X, Han J, Liu W. 2022. Microcapsule delivery systems of functional ingredients in infant formulae: Research progress, technology, and feasible application of liposomes. Trends Food Sci Technol 119:36-44.

Warnakulasuriya SN, Nickerson MT. 2018. Review on plant protein–polysaccharide complex coacervation, and the functionality and applicability of formed complexes. J Sci Food Agric 98:5559-5571.

Xiao S, Ahn DU. 2023. Co-encapsulation of fish oil with essential oils and lutein/curcumin to increase the oxidative stability of fish oil powder. Food Chem 410:135465.

Xu K, Zhao Z, Guo M, Du J. 2019. Conjugation between okra polysaccharide and lactoferrin and its inhibition effect on thermal aggregation of lactoferrin at neutral pH. LWT-Food Sci Technol 107:125-131.

Xu Y, Yang N, Yang J, Hu J, Zhang K, Nishinari K, Phillips GO, Fang Y. 2020. Protein/polysaccharide intramolecular electrostatic complex as superior food-grade foaming agent. Food Hydrocoll 101:105474.

Yan M, Wang Y, Shen X, Dong S, Diao M, Zhao Y, Zhang T. 2022. Enhanced foaming properties of lactoferrin by forming functional complexes with ginsenoside Re and Rb1. Food Hydrocoll 123:107159.

Yang N, Li Y, Xing F, Wang X, Li X, Li L, Yang J, Wang Y, Zhang M. 2021. Composition and structural characterization of

pectin in micropropagated and conventional plants of *Premma puberula* Pamp. Carbohydr Polym 260:117711.

Zhang Q, Dong H, Gao J, Chen L, Vasanthan T. 2020. Field pea protein isolate/chitosan complex coacervates: Formation and characterization. Carbohydr Polym 250:116925.

Zhang X, Chen M, Wang N, Luo J, Li M, Li S, Hemar Y. 2024. Conjugation of chitopentaose with *β*-lactoglobulin using Maillard reaction, and its effect on the allergic desensitization *in vivo*. Int J Biol Macromol 258:128913.

Zheng J, Gao Q, Tang C, Ge G, Zhao M, Sun W. 2020. Heteroprotein complex formation of soy protein isolate and lactoferrin: Thermodynamic formation mechanism and morphologic structure. Food Hydrocoll 100:105415.

Zhu SM, Lin SL, Ramaswamy HS, Yu Y, Zhang QT. 2017. Enhancement of functional properties of rice bran proteins by high pressure treatment and their correlation with surface hydrophobicity. Food Bioprocess Technol 10:317-327.